WILEY | Hindawi

Research Article

Degradation Characteristics and Mechanism of Black Sandy Dolomite with Fluid Added in a Mechanical Test

Xin Liao,[1,2] Qi Xu [ID],[3] Sixiang Ling,[1,2] Angran Tian [ID],[3] and Qiang Tang [ID][3]

[1]Faculty of Geosciences and Environmental Engineering, Southwest Jiaotong University, Chengdu 611756, China
[2]MOE Key Laboratory of High-Speed Railway Engineering, Southwest Jiaotong University, Chengdu 611756, China
[3]School of Rail Transportation, Soochow University, Suzhou 215131, China

Correspondence should be addressed to Angran Tian; gangguo@126.com and Qiang Tang; tangqiang@suda.edu.cn

Sandy dolomite, being a soluble rock, is prone to dissolution and erosion caused by groundwater, leading to the formation of underground caves and fractures. This may result in geological disasters such as ground subsidence and collapse. In this paper, the changes and mechanical properties of black sandy dolomite after hydrochemistry are studied. A semi-immersion test with different concentrations of iron sulfate solution was carried out to simulate the water-rock interaction in different water environments. After that, scanning electron microscope (SEM) results could reflect the dissolution and pore development of rock by the effect of water-rock interaction from the microscopic. Water-rock interaction enlarges cracks in rocks and dissolves pyrite, carbonate minerals, and other components, reducing the cementation between particles. The change in the mechanical properties of black sandy dolomite under water-rock chemical interaction was revealed by uniaxial compression test. The mechanical properties of the samples exhibit varying degrees of deterioration, with strain increased ranging from 4.96 to 29.58%. The brittleness index modified (BIM) values for each sample ranged from 5.20 to 6.20%, all of which are larger than 4.70% in the natural state.
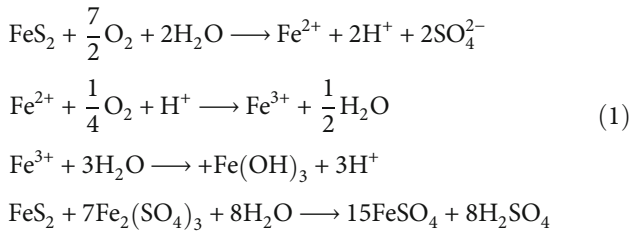
1. Introduction

Sandy dolomite, a sedimentary rock primarily composed of dolomite (a calcium magnesium carbonate mineral) and sand-sized particles [1], is known for its abundant presence of pores and fissures, making it susceptible to erosion and dissolution by groundwater [2, 3]. This rock type is frequently utilized in geology as a significant layer for underground water storage and transportation purposes [4]. However, its solubility and fissure characteristics also render it prone to geological hazards, including ground subsidence, collapse, and damage [5]. In the context of preventing and controlling geological hazards in mountainous regions, investigating the characteristics and mechanisms of sandy dolomite holds great significance for the mitigation of landslides and rock collapses [6, 7].

With increasing concerns regarding engineering construction issues associated with sandy dolomite strata, the investigation of degradation caused by water-rock interaction has emerged as a forefront topic in the field of engineering geology. During the weathering process, sulfide minerals and organic matter present in sandy dolomite undergo oxidation in an oxygen-rich water environment, resulting in the formation of a complex acidic water environment [8, 9]. Consequently, water dissolution leads to the depletion of certain minerals, while the formation of new minerals occurs in their original positions, thereby altering the distribution of pores and stress within the rocks [10]. This aqueous environment further accelerates the weathering of primary minerals, leading to the rapid disintegration of rocks and subsequent modifications to their composition and structure [11]. Ultimately, the chemical weathering of

the rock mass can result in the deterioration of its physical and mechanical properties.

Sandy dolomite contains a significant amount of organic matter and sulfide minerals, particularly pyrite, which plays a crucial role in water-rock interaction. Pyrite surfaces do not achieve automatic charge compensation, leading to the formation of polar surfaces with excess charges. These polar surfaces exhibit instability and high surface activity. They readily form bonds with ions or molecules in the surrounding medium to compensate for the excess charges in the suspension, resulting in surface oxidation reactions [12, 13]. In an acidic environment, the oxidation reaction of pyrite can be expressed as follows:

$$
\begin{aligned}
&\text{FeS}_2 + \frac{7}{2}\text{O}_2 + 2\text{H}_2\text{O} \longrightarrow \text{Fe}^{2+} + 2\text{H}^+ + 2\text{SO}_4^{2-} \\
&\text{Fe}^{2+} + \frac{1}{4}\text{O}_2 + \text{H}^+ \longrightarrow \text{Fe}^{3+} + \frac{1}{2}\text{H}_2\text{O} \\
&\text{Fe}^{3+} + 3\text{H}_2\text{O} \longrightarrow +\text{Fe(OH)}_3 + 3\text{H}^+ \\
&\text{FeS}_2 + 7\text{Fe}_2(\text{SO}_4)_3 + 8\text{H}_2\text{O} \longrightarrow 15\text{FeSO}_4 + 8\text{H}_2\text{SO}_4
\end{aligned}
\tag{1}
$$

The reactions involved in water-rock interaction continue to cycle, resulting in intensification. Research indicates that Fe^{3+} ions, rather than O_2, are the most significant oxidizing agents in the process of pyrite oxidation [14, 15]. Aqueous solutions containing ferric ions can accelerate the oxidation of pyrite, leading to an increased concentration of hydrogen ions in the water environment of the rock and subsequent acidification [16]. Therefore, investigating iron ions, which are among the primary factors influencing the water-rock interaction of rock strata, holds theoretical importance in exploring the degradation patterns of the mechanical properties of sandy dolomite strata.

By applying the energy mechanism, the process of energy absorption, transformation, and release in rocks can be studied more effectively, leading to a more comprehensive understanding of the degradation process of rocks. Previous studies have systematically explained the process of rock deformation and failure and the characteristics of energy transformation [17, 18]. The energy absorbed and transformed from the outside is divided into dissipative energy and releasable elastic energy. Dissipated energy can be used to describe the new plastic deformation and internal damage of rock mass, which is the main cause of rock strength loss [19, 20]. The releasable elastic strain energy can be released during unloading.

In this paper, the effect of water-rock interaction on the deterioration of sandy dolomite was studied, taking black sandy dolomite as the research object. Semi-immersion tests were conducted under various ferric sulfate concentrations to simulate the effects of different water environments. Subsequently, uniaxial compression tests were performed to determine the changes in the mechanical properties of the samples due to the chemical effects of water-rock interaction. Based on the energy mechanism, the energy changes of rocks under uniaxial compression were analyzed.

2. Materials and Methods

2.1. Sampling and Preparation.
The rock samples studied in this paper were selected from the lower Cambrian black rock in Chengkou County, Chongqing, China. Due to the high levels of rainfall and hot summer temperatures in the local area, the rock strata distributed in the study area have strong water-rock interaction. As a result of abundant rainfall, the surface of the rock mass was visibly fractured and denuded. The rock mass was coated with a yellow substance, which was speculated to be the oxide formed by the replacement of iron ions due to the water-rock interaction.

The black sandy dolomite rock blocks were selected and prepared into standard cylindrical samples with dimensions of φ50 mm × 100 mm, following the ASTM D4543 standard [21]. Using ultrasonic velocity measurement, eight samples with uniform internal structure were chosen. In order to provide an objective assessment of the sample properties, three samples were selected for the determination of their physical and chemical properties.

The mineral analysis results obtained through X-ray diffraction (XRD) measurements are presented in Table 1 and Figure 1, providing valuable insights into the mineral composition of the tested black sandy dolomite samples. The dominant minerals observed in the samples are dolomite, accounting for 46.60-52.40% of the composition, and quartz, comprising 31.70-36.80% of the mineral content. Additionally, minor constituents such as pyrite (3.60-4.60%), plagioclase (1.60-2.90%), and illite (1.91-3.59%) were identified. The samples also contain trace amounts of chlorite (0.36-0.59%), kaolinite (0.37-0.59%), and other unidentified minerals.

The chemical composition analysis of the black sandy dolomite samples was conducted using PW2424 X-ray fluorescence spectrometer (XRF), and the results are presented in Table 2. The chemical composition of the samples is mainly SiO_2 (32.00-36.37%), followed by CaO (16.45-18.55%), with MgO content of 11.55-12.95%. The contents of Al_2O_3, SO_3, and Fe_2O_3 are 2.17-3.30%, 2.25-2.80%, and 1.39-1.47%, respectively. Other chemical compositions are relatively low. This indicates that there are some pyrite contained in the black sandy dolomite samples as well. The loss on ignition (LOI) is 25.64-28.98%, indicating that there is high content of inorganic carbonate in the rock.

2.2. Experiments

2.2.1. Semi-immersion Test.
After drying and vacuuming the rock samples, they were immersed in solutions of $Fe_2(SO_4)_3$ at different concentrations for this study. Acid-proof plastic boxes were used as containers, with four groups consisting of two soaking samples per group. The immersion solution in the simulation test consisted of deionized water and sulfuric acid, with Fe^{3+} concentrations of 1 g/L, 1.5 g/L, 2 g/L, and 2.5 g/L, labeled as A, B, C, and D, respectively, in ascending order of concentration. The semi-immersion experiment is shown in Figure 2.

According to the empirical formula of the oxidation rate of bulk pyrite, the concentration of Fe^{3+} produced during

TABLE 1: Mineral composition of the samples.

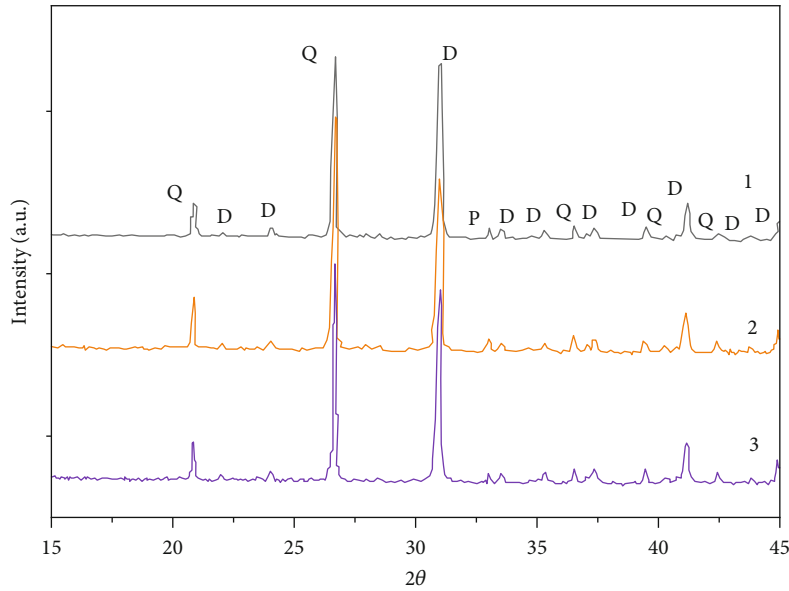| Sample	Quartz	Plagioclase	Pyrite	Dolomite	Illite	Kaolinite	Chlorite	Others
1	31.70	2.20	4.60	52.40	1.91	0.46	0.36	6.38
2	36.80	2.90	5.30	46.60	3.02	0.34	0.59	4.45
3	33.80	1.60	3.60	51.80	3.59	0.46	0.46	4.69
Average	34.10	2.23	4.50	50.27	2.84	0.42	0.47	5.17

FIGURE 1: X-ray diffraction results of the samples. D: dolomite; Q: quartz; P: pyrite.

TABLE 2: Chemical composition of the samples.

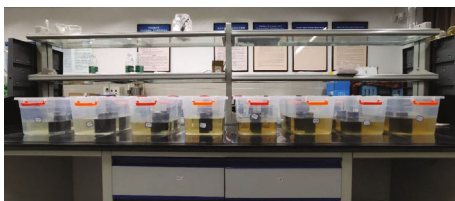| Sample	SiO_2	TiO_2	Al_2O_3	K_2O	MgO	Fe_2O_3	CaO	P_2O_5	Na_2O	SO_3	Cr_2O_3	BaO	LOI
1	32.83	0.13	2.17	0.52	12.85	1.44	18.30	0.06	0.16	2.27	<0.01	0.03	28.54
2	36.37	0.18	3.30	0.87	11.55	1.47	16.45	0.09	0.27	2.80	<0.01	0.05	25.64
3	32.00	0.14	2.22	0.58	12.95	1.39	18.55	0.09	0.16	2.25	<0.01	0.02	28.98
Average	33.73	0.15	2.56	0.66	12.45	1.43	17.77	0.08	0.20	2.44	<0.01	0.03	27.72

FIGURE 2: Semi-immersion experiment.

the oxidation and acid erosion process of black sandy dolomite differs by four orders of magnitude from the Fe^{3+} concentration in the immersion solution. This difference has a weak impact on the test process and can be ignored [22–24]. Therefore, the chosen iron ion concentrations in the immersion solution for this paper are reasonable and feasible.

Before the test, the rock samples underwent vacuum freeze-drying for one hour using a vacuum freeze-dryer. This process created a negative pressure within the rock mass, ensuring that the soaking liquid entered the rock mass through the cracks. The initial pH value of the precipitate was approximately 2.2, so the pH value of the immersion solution was set to 2.

During the test, the electronic conductivity and pH of each group of solutions were periodically measured. Initially, measurements were taken three times a day at 6-hour intervals, and subsequently, measurements were taken twice a day at 12-hour intervals. After the semi-immersion test, the samples were removed for the mechanical test.

2.2.2. Scanning Electron Microscopy Analysis. The rock samples were initially cleaned to eliminate surface impurities. Subsequently, they were processed into small pieces of approximately $1\,cm^3$ using a cutting machine. The surfaces of these samples were then polished to obtain smooth flakes suitable for argon ion polishing. These samples were polished in a LEICA EM RES102 argon ion polishing instrument. The polished samples were thoroughly cleaned with deionized water and dried for 24 h in a drying box with the temperature set at 60°C. After the rock sample was polished by argon ions, they were fixed on the surface of the coin to ensure the smooth placement of the rock sample on the scanning electron microscope platform, and then, the rock sample was observed and analyzed by scanning electron microscopy (QUanta-Fec250). Lastly, a platinum coating was applied to the surface of the rock samples observed under the scanning electron microscope. This was accomplished by placing the samples into a platinum deposition instrument, ensuring optimal electrical conductivity through a platinum injection time of 60 seconds.

2.2.3. Uniaxial Compression Experiment. After 41 days of soaking in different ferric sulfate solutions, the samples underwent uniaxial compression testing using a YZW-Y series microcomputer-controlled electrohydraulic servo pressure testing machine, with a loading rate of 0.5 MPa/s. The test was conducted until the sample was completely destroyed, and the stress-strain parameters of each sample were recorded.

3. Results and Discussion

3.1. Oxidation-corrosion morphology of the samples. The change of the samples at four different concentrations is similar. Typical changes in the process of immersion are described as follows.

The rock samples were immersed in a liquid solution with the top surface positioned approximately 1 cm above the water level. Upon immersion, bubbles were observed in the lower portion of the solution at all concentrations. After 3 days, a slight cloudiness was noticeable in the soaking solution compared to its initial state. By the fourth day, the sample with a concentration of 1 g/L exhibited an increased pH value, accompanied by additional precipitation at the bottom of the solution. Precipitation in the form of white substances was observed in the wetted regions above the liquid level for all rock samples, consistently appearing at the boundary between the wet and dry areas surrounding the rock samples.

After 14 days, the height of the immersion solution within the rock samples had increased by approximately 1 cm due to capillary action, and an increased amount of flocculent or needle-like white precipitates was observed. Some of the precipitates transitioned from white to a yellow-brown color. At the 20-day mark, the soaking solution further penetrated the internal pores of the rock samples, resulting in significant precipitation from the immersed regions. Approximately half of the white precipitates turned yellow-brown in alignment with the direction

of solution infiltration. Over time, noticeable dissolution phenomena occurred within the wetted portions of the rock samples.

By the 34th day, the wetted regions of the rock samples displayed the appearance of yellow-brown material, with the coverage area gradually expanding. As more precipitates migrated through the pores in the direction of the solution, the surface exhibited undulations, and a few instances of exfoliation and discrete particles could be observed at the bottom of the solution. After 41 days, no visible precipitate was observed on the immersed surface of the rock samples. However, the portion above the liquid level was coated with a yellow-brown precipitate. Figure 3 provides a depiction of the typical etching characteristics observed in the samples.

3.2. pH and Electric Conductivity. Electric conductivity (EC) is a measure of solution conductivity and is influenced by the properties of ions present in the solution. The observed increase in conductivity can be attributed to the ongoing oxidation of pyrite, resulting in the production of various ions. Simultaneously, the hydrogen ions generated during the oxidation process react with other minerals within the rock sample, causing their dissolution and the formation of additional soluble ions. Consequently, the conductivity value is further elevated. The augmentation of electrical conductivity exhibits a positive correlation with the extent of water-rock interaction.

The relationship curves of EC and pH values of the samples in hydrochemical solutions with different concentrations with experimental time are shown in Figure 4. The data shown in the figure are the average values of the two samples in each experiment group. The EC changes in different concentrations of aqueous chemical solution in different time periods were consistent. In the early stage of the test, the soaking solution directly contacted the surface of the rock sample, and the soaking fluid entered the sample along with the pores. The water-rock reaction was severe, and rock-forming minerals and cementation were dissolved. Soluble minerals in the rock sample begin to decompose, producing ions into the immersion solution, such as Fe^{2+} and Mg^{2+}. Macroscopically, the conductivity of the soaking fluid increased. With the passage of oxidation acid etching time, the conductivity of the soaking solution increased gradually, and when it increased to a certain value, the increasing rate decreased to different degrees and finally tended to a certain stable value.

To ensure that the pH value was kept within a stable range during the test, when the pH value rose to 2.3, an appropriate amount of sulfuric acid solution was added to the soaking solution to adjust the pH value to the initial value of 2. The EC and pH values increased and decreased rapidly in the early stage in group A. At 25 h, the EC value reached a maximum of 6.8 mS/cm, and the pH value reached a minimum of 1.6. Then, the EC value began to decrease with partial fluctuation, and the pH value began to rise. In groups B, C, and D, the trends of both were similar; the EC value increased slowly, and the pH value decreased slowly. After 25 h, EC and pH fluctuated occasionally but
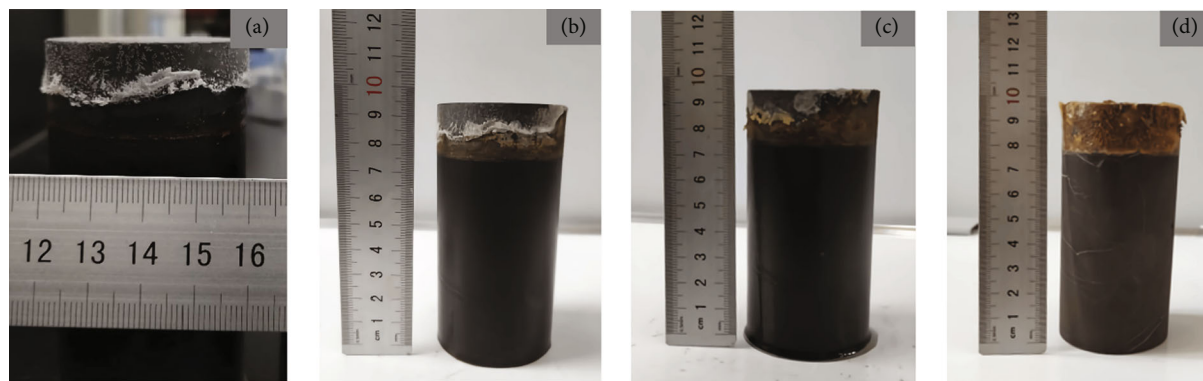
FIGURE 3: Group A oxidation acid etching characteristics: (a) day 4; (b) day 20; (c) day 34; (d) day 41.

generally tended to be stable, and the conductivity stabilized at approximately 3.3, 5.1, and 6.2 mS/cm, respectively.

After 500 hours of testing, the EC value and pH value of the soaking solution in the test groups were stable. It is speculated that pyrite in the rock is completely dissolved and the chemical reactions reach equilibrium. The conductivity of the four groups increased from 3.2 to 9.8 mS/cm, 2.7 to 8.2 mS/cm, 4.0 to 9.2 mS/cm, and 4.6 to 9.1 mS/cm, respectively. The pH values of the four groups were kept at about 2.0, 2.1, 2.1, and 2.0, while the electrical conductivity increased with growth rates of 206%, 203%, 130%, and 97%, respectively. The change in conductivity decreases with increasing immersion concentration. This indicates that with the increase in the concentration of Fe^{3+} in the soaking solution, the water-rock chemical interaction weakens in the same period. The rate of ion generation is also slow, which makes the change range of EC smaller, leading to less consumption of H^+ and a smaller rise rate of pH. It is speculated that the complexes formed by Fe^{3+} with water and dissolved oxygen cover the surface of rock samples in the form of thin films, which inhibit the dissolution rate of diagenetic minerals. This prevents further chemical reactions, giving the rock some protection [25, 26]. The control group with the same concentration of iron ions and different immersion heights showed a similar change trend in EC, indicating that the immersion height has little effect on the water-rock interaction of black sandy dolomite.

3.3. Characteristics of Microstructure after Water-Rock Interaction. The samples of black sandy dolomite were analyzed by scanning electron microscopy after soaking in solutions for 41 days. Pores and fissures in the black sandy dolomite were observed, as well as the microstructure and the cementation between the mineral particles.

The internal microstructure before water-rock interaction of the sample is shown in Figure 5(a). The overall structure of the black sandy dolomite is closely connected, and the main frame is jointly constructed of dolomite and quartz. The overall structure of the rock and the clay minerals is layered.

Figure 5(b) shows the internal pore diagram of black sandy dolomite in natural state. The size and shape of microscopic particles are irregular, and the structure between particles is loose. Inside the rock, there are many pores of different sizes with irregular shapes (red arrows). The pores are a few microns in diameter, much smaller than the minerals in the rock sample. At the same time, honeycomb aggregates were observed, which were inferred to be pyrite by X-ray energy-dispersive spectrometry. Pyrite on the surface of rock samples is easily dissolved into fine particles, which are further decomposed into ions to improve the conductivity of the solution.

Erosion and fissures occurred in the samples, as shown in Figure 5(c), resulting in mineral loss and disintegration. Pore water carries the ions released by minerals to move into the cracks of rock mass. After the ion concentration reaches saturation in the open area of the cracks, mineral redeposition will occur. During this process, the concentration of ions in the solution increases, resulting in the increase of EC value. Chemical dissolution in the narrow fissure widens the opening, changes the cementation between mineral particles, and reduces the mechanical properties. In acidic environments, all the samples have strong dissolution phenomena, mainly manifested as dissolution and expansion along the intergranular pores and all kinds of cracks and cavities, and finally connected to a certain extent. After these reactions, the solution pores and gaps are beaded. Figure 5(d) shows that the pyrite particles are eroded away and the original structure turns into holes after water-rock interaction.

Scanning electron microscopy analysis reveals that the microdissolution process of dolomite primarily occurs along the dolomite grains, crystalline pores, and crystal interfaces. Dissolution initially takes place at crystal cleavage fissures, contact points between dolomite crystals, and within and around sand patches. This results in a gradual deterioration of the internal structure of dolomite. The pores gradually enlarge and extend as the dissolution progresses. Crystal detachment during the process weakens the interconnection between dolomite crystals, leading to a loosening of the structure and the eventual formation of a powdery substance. Thus, water-rock interaction has a significant impact on the micromorphological characteristics of the rock samples.
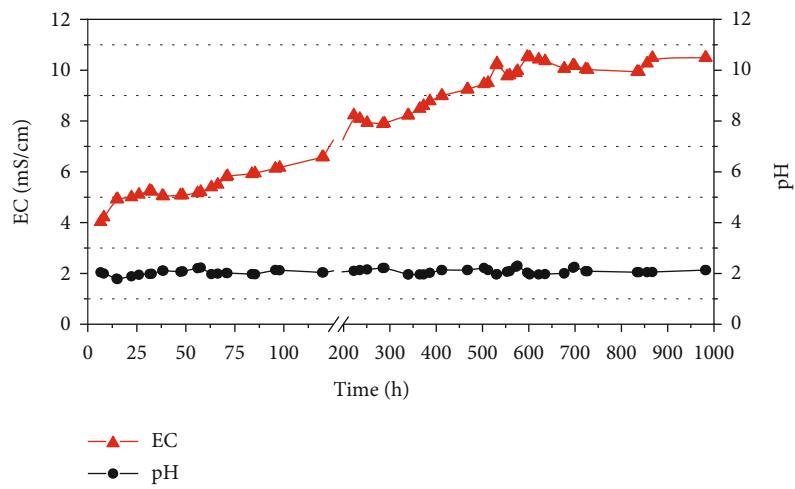
3.4. Uniaxial Compression Experiment Results. The results of the uniaxial compression test indicate that the failure mode of the rock samples is brittle failure. The stress-strain curve
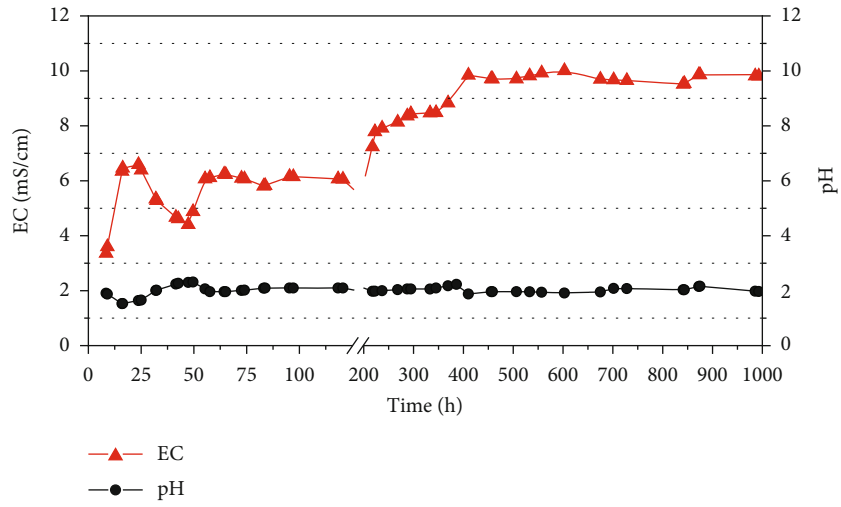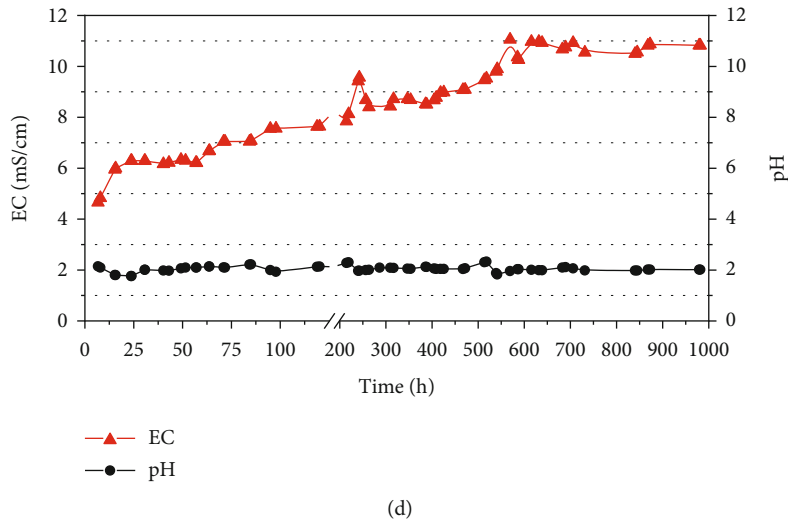
(a)
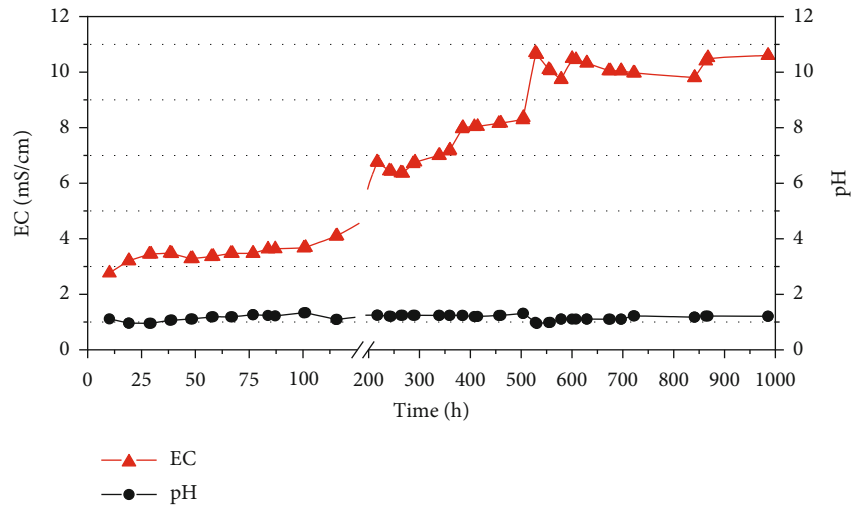
(b)

(c)

Figure 4: Continued.

(d)

FIGURE 4: Conductivity and pH value of the samples: (a) group A; (b) group B; (c) group C; (d) group D.
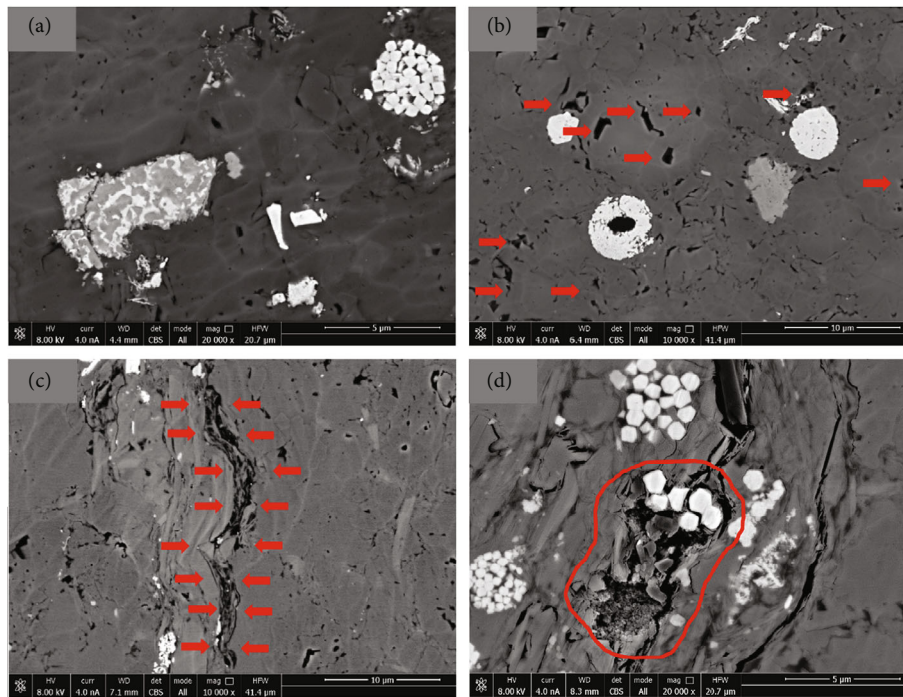

FIGURE 5: SEM images of the samples before and after water-rock interaction. Before water-rock interaction: (a) overall structure and (b) internal pores. After water-rock interaction: (c) enlargement of pores and (d) pyrite corrosion.

of the samples after acid etching with different concentrations of Fe^{3+} is shown in Figure 6.

The initial compression section of the uniaxial compression stress-strain curve of a rock sample displays an upward concave shape, and its length is indicative of the sample's internal defects and void development. After chemical corrosion, the upward concave section of the sample is lengthened. The length and degree of the upper sag can reflect the pore development of rock. The compaction section of the sample increased obviously. The softening effect of the

chemical solution significantly impacts the elastic and yield stages of the curve, with the elastic stage being shorter after chemical corrosion than under natural conditions.

At the stage of plastic deformation, the peak point strain can reflect the amount of deformation when the rock is damaged. The mechanical and deformation parameters of specimens obtained by uniaxial compression test are shown in Table 3. With the increase in acidity of the chemical solution. The axial strain increases when the peak point is reached. After soaking in chemical solution, the axial strain
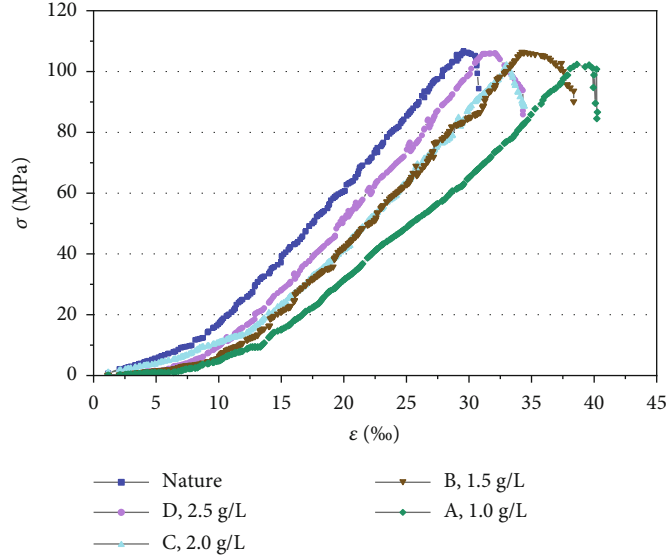
Figure 6: Stress-strain curves of the samples.

at the peak point of each sample is greater than that in the natural state.

The degradation of mechanical indexes of the sample under different Fe^{3+} ion concentrations is as follows: compared with the unsoaked samples, the peak strength of groups A, B, C, and D decreased by 4.18%, 0.19%, 2.93%, and 0.64%; the peak strain increased by 29.58%, 14.11%, 12.42%, and 4.96%; and the elastic modulus decreased by 16.00%, 2.96%, 6.98%, and 1.88%, respectively. Different concentrations of immersion solution have different corrosion effects on the samples. With increasing Fe^{3+} ion concentration, the degradation rate of the strength parameter decreased. If the concentration of Fe^{3+} increases, Fe^{3+} forms a film on the surface of the sample, the contact surface between sample and solution was reduced, and the dissolution rate is inhibited [27–29].

4. Energy Mechanism under Uniaxial Compression

In the process of the uniaxial compression test, the rock deforms until it is destroyed by an external load. It is assumed that there is no heat exchange in the process of deformation, and the external force works on the rock with input energy U. That includes the elastic strain energy released at the time of failure and the dissipated energy of the rock [25].

$$U = U^e + U^d, \tag{2}$$

where U^e is the releasable elastic strain energy and U^d is the dissipated energy.

The relationship between dissipative energy U^d and releasable elastic energy U^e is shown in Figure 7. The dissipated energy of damage and plastic deformation U^d in the

Table 3: Strength and deformation parameters of the samples under uniaxial conditions.

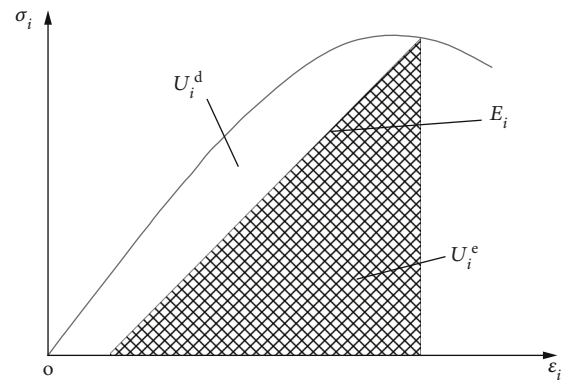| Group	Peak strength (MPa)	Peak strain (‰)	Elasticity modulus (GPa)
A	102.16	38.54	3.87
B	106.41	33.94	4.47
C	103.50	33.44	4.28
D	105.94	31.22	4.52
Nature	106.62	29.75	4.60

Figure 7: Quantitative relationship between U^e and U^d.

forming element is numerically equal to the area formed by the stress-strain relationship curve and the unloading elastic modulus. The area of the shaded part represents the value of the releasable elastic strain energy U^e, which is the elastic strain energy released by the rock mass after unloading.

TABLE 4: Average plastic deformation and BIM.

Group	A	B	C	D	Nature
Concentration (g/L)	1.0	1.5	2.0	2.5	/
BIM (%)	6.20	5.60	5.90	5.20	4.70
U_p (mm)	1.22	1.02	0.93	0.78	0.65

The energy of each part in the principal stress space can be represented as [26]

$$U = \int_0^{\varepsilon_1} \sigma_1 d\varepsilon_1 + \int_0^{\varepsilon_2} \sigma_2 d\varepsilon_2 + \int_0^{\varepsilon_3} \sigma_3 d\varepsilon_3,$$

$$U^e = \frac{1}{2}\sigma_1 d\varepsilon_1^e + \frac{1}{2}\sigma_2 d\varepsilon_2^e + \frac{1}{2}\sigma_3 d\varepsilon_3^e, \quad (3)$$

$$U^d = U - U^e.$$

In this formula, U is the work done by the principal stress in the direction of the principal stress; ε_i ($i = 1, 2, 3$) is the strain in three principal stress directions; ε_i^e ($i = 1, 2, 3$) is the elastic strain in three principal stress directions.

In practical engineering applications, the releasable elastic strain energy can be written as follows [30, 31]:

$$U^e = \frac{\sigma_1^2 + \sigma_2^2 + \sigma_3^2 - 2\mu(\sigma_1\sigma_2 + \sigma_2\sigma_3 + \sigma_3\sigma_1)}{2E_u}, \quad (4)$$

where E_u is the unloading elastic modulus.

At present, a large number of studies show that the initial elastic modulus E_0 is generally used to replace the unloading elastic modulus E_u in calculating the elastic strain energy that can be released [32–34]. In the uniaxial compression test, only the axial stress ε_1 works on the sample, and the principal stress in the other directions is 0. Therefore, the above formula can be written as

$$U = \int_0^{\varepsilon_1} \sigma_1 d\varepsilon_1, \quad (5)$$

$$U^e = \frac{1}{2}\sigma_1 d\varepsilon_1^e, \quad (6)$$

$$U^d = U - U^e = \int_0^{\varepsilon_1} \sigma_1 d\varepsilon_1 - \frac{\sigma_1^2}{2E_0}. \quad (7)$$

The amount of plastic deformation can be expressed by the value of the brittleness index modified (BIM) [35, 36]:

$$\text{BIM} = \frac{U^d}{U^e}, \quad (8)$$

where U^d and U^e represent the dissipated energy and releasable elastic energy of the sample at the peak stress.

The total plastic deformation of the sample in the progressive failure process under uniaxial compression can be calculated by the formula below [37]:

$$U_p = L\left(\varepsilon - \frac{\sigma}{E}\right), \quad (9)$$

where U_p is the total plastic deformation of the sample, L is the length of the sample, ε is the axial strain, E is the elastic modulus, and σ is the axial compressive stress.

According to Equations (8) and (9), the average plastic deformation amount and brittleness correction index value of the sample at the peak stress before failure can be obtained, as shown in Table 4.

As shown in Table 4, the BIM of the sample in the natural state is 4.70%, while those of the samples after soaking are 6.20%, 5.60%, 5.90%, and 5.20%. That is greater than the value of the rock in the natural state and decreases with the increase in the concentration of solution. This indicates that after oxidizing acid corrosion, the samples softened, the ductility enhanced and brittleness weakened. The degree of softening decreased with increasing aqueous chemical solution concentration. The average plastic deformation of groups A, B, C, and D is 1.22 mm, 1.02 mm, 0.93 mm, and 0.78 mm, which are larger than the average plastic deformation of the natural rock (0.65 mm). This demonstrates that the variation law of BIM is the same as the average plastic deformation, so the energy mechanism can be used to characterize the chemical corrosion of rock. The larger the brittleness correction index value is, the deeper the mechanical properties of the sample deteriorate under the effect of chemical corrosion.

According to Equation (5)-Equation (7), the curves of the relationship between the strain energy of each part and axial strain can be obtained, which were affected by chemical corrosion at different concentrations, as shown in Figure 8.

It can be seen intuitively from Figure 8 that the accumulation and transformation patterns of the absorbed strain energy in various components are generally consistent in black sandstone limestone specimens in their natural state and after chemical corrosion. However, the evolution of energy in the process of deformation and failure of the black sandy dolomite samples in the hydrochemical solution corrosion is still obviously different from that in the natural state. The increase rates of absorbed total strain energy and releasable elastic strain energy in the saturated state after chemical corrosion are lower than those in the natural state. With the same axial strain, the strain energy U and the released elastic strain energy U^e are both larger than those after chemical corrosion, indicating that the chemical solution has a significant effect on them. After the peak value
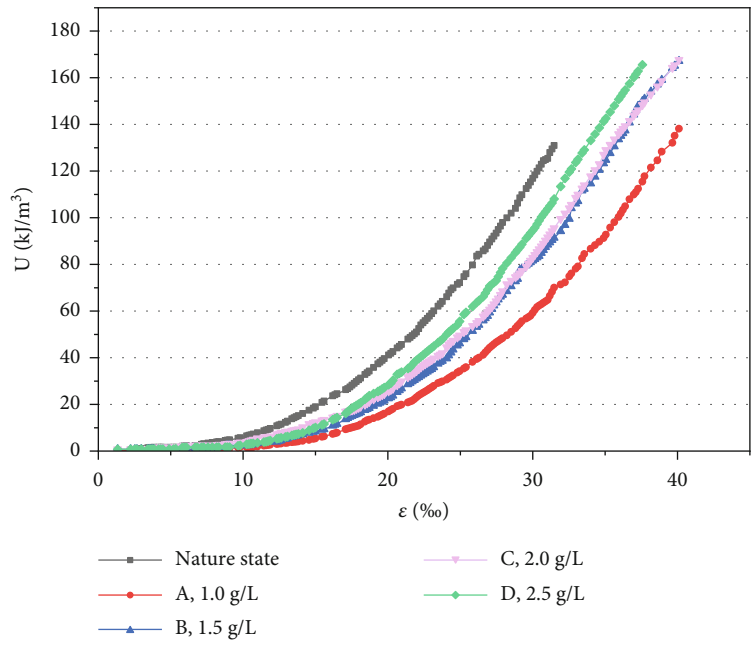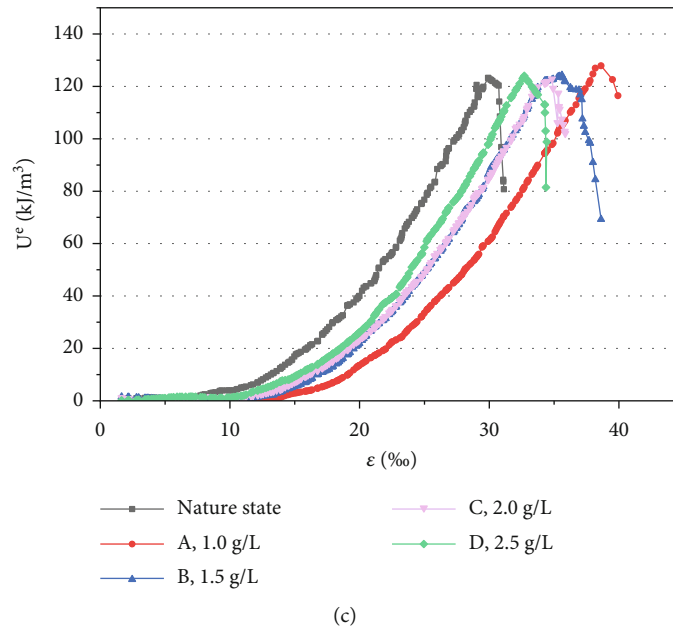
(a)
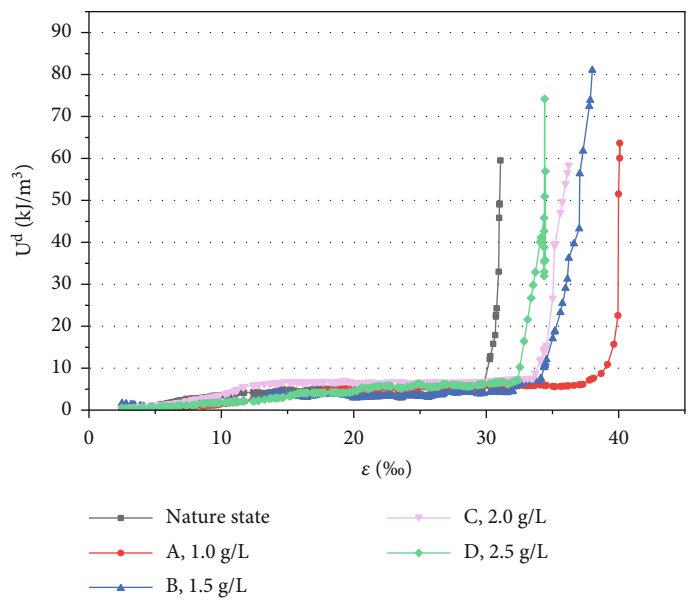
(b)

FIGURE 8: Continued.

(c)

FIGURE 8: Curves of axial strain and energy: (a) total strain energy; (b) dissipation energy; (c) releasable energy.

point, the energy absorption from the external environment decreases to varying degrees for both natural corrosion and chemical corrosion, but the decrease is more significant under chemical corrosion.

5. Conclusions

The semi-immersion test and uniaxial compression test of black sandy dolomite at different concentrations were carried out, and the mechanical properties of rock under different chemical damage states were analyzed combined with the energy mechanism. The specific results are as follows:

(1) The morphological characteristics of oxidizing acid erosion of black sandy dolomite were obtained through the semi-immersion test of chemical solutions with different Fe^{3+} concentrations. Results showed that water-rock interaction was more significant when the concentration of iron ions was low. The electrical conductivity (EC) value increased rapidly in 1 g/L solution and reached its maximum after approximately 25 hours, earlier than other concentrations. Moreover, the hydrogen ion consumption capacity is weak, and the pH value increases more slowly

(2) Through uniaxial compression tests of the samples corroded by chemical solutions of different concentrations, the stress-strain relationship curves of the whole process were obtained. Under the natural state of rock in water after chemical etching, the peak strength of the samples decreased to varying degrees, and the peak strain increased to different extents, with a decreasing trend as the concentration of Fe^{3+} increased. The maximum increasement of

strain reached 29.58% at a concentration of 1 g/L iron ions, and the minimum was 4.96% at 2.5 g/L

(3) The variations in mechanical properties of the rock under uniaxial compression have been derived from an energy-based perspective by analyzing the stress-strain curves. With increasing chemical solution concentration, the strain energy of each characteristic point of the rock sample decreases, and the U_d/U value, brittleness correction index, and average plastic deformation also decrease. BIM reaches the highest value of 6.20% at 1 g/L, and U_p also reaches the maximum value of 1. The variation range of the elastic strain energy (U_e) value is small, suggesting that the elastic properties of the rock have not changed significantly during the process of energy absorption

Data Availability

The data used to support the findings of this study are available from the corresponding authors upon request.

Conflicts of Interest

The authors declare that they have no competing interests.

Acknowledgments

References

[1] M. Wang, W. Xu, H. Mu, J. Mi, Y. Wu, and Y. Wang, "Study on construction and reinforcement technology of dolomite sanding tunnel," *Sustainability*, vol. 15, p. 9217, 2022.

[2] P. Zhou, Y. Fan, F. Zhou, F. Wu, Y. Yong, and Z. Wang, "Disaster mechanism of tunnel face with large section in sandy dolomite stratum," *Engineering Failure Analysis*, vol. 131, article 105905, 2022.

[3] V. Chander, D. Tewari, V. Negi, R. Singh, and L. Aleya, "Structural characterization of Himalayan black rock salt by SEM, XRD and in-vitro antioxidant activity," *Science of the Total Environment*, vol. 748, article 141269, 2020.

[4] Y. Jiang, P. Zhou, F. Zhou et al., "Failure analysis and control measures for tunnel faces in water-rich sandy dolomite formations," *Engineering Failure Analysis*, vol. 138, article 106350, 2022.

[5] R. Attia and G. Awny, "Leaching characterisations and recovery of copper and uranium with glycine solution of sandy dolomite, Allouga area, South Western Sinai, Egypt," *International Journal of Environmental Analytical Chemistry*, pp. 1–14, 2021.

[6] X. Liao, X. Wu, B. Zhu, and F. Jun, "Study on the characteristics of black strata geochemical weathering and its disaster-causing mechanism," *Disaster Advances*, vol. 5, no. 4, pp. 1558–1562, 2012.

[7] L. Li, C. Xu, X. Yao et al., "Large-scale landslides around the reservoir area of Baihetan hydropower station in Southwest China: analysis of the spatial distribution," *Natural Hazards Research*, vol. 2, no. 3, pp. 218–229, 2022.

[8] O. Farkas, S. Siegesmund, T. Licha, and Á. Török, "Geochemical and mineralogical composition of black weathering crusts on limestones from seven different European countries," *Environmental Earth Sciences*, vol. 77, no. 5, pp. 175–184, 2018.

[9] M. W. Saaltink, C. Domenech, C. Ayora, and J. Carrera, "Modelling the oxidation of sulphides in an unsaturated soil," *Geological Society, London, Special Publications*, vol. 198, no. 1, pp. 187–204, 2002.

[10] J. Srodo, J. Szulc, and A. Anczkiewicz, "Weathering, sedimentary and diagenetic controls of mineral and geochemical characteristics of the vertebrate-bearing Silesian Keuper," *Clay Minerals*, vol. 49, no. 4, pp. 569–594, 2014.

[11] X. Liao, M. Chigira, Y. Matsushi, and X. Wu, "Investigation of water–rock interactions in Cambrian black shale via a flow-through experiment," *Applied Geochemistry*, vol. 51, pp. 65–78, 2014.

[12] E. Forbes, L. Smith, and M. Vepsalainen, "Effect of pyrite type on the electrochemistry of chalcopyrite/pyrite interactionsm," *Physicochemical Problems of Mineral Processing*, vol. 54, no. 4, pp. 1116–1129, 2018.

[13] M. Berta, F. Dethlefsen, M. Ebert, K. Gundske, and A. Dahmke, "Surface passivation model explains pyrite oxidation kinetics in column experiments with up to 11 bars p (O_2)," *Environmental Earth Sciences*, vol. 75, no. 16, pp. 1–13, 2016.

[14] Y. Liu, Z. Dang, P. Wu, J. Lu, X. Shu, and L. Zheng, "Influence of ferric iron on the electrochemical behavior of pyrite," *Ionics*, vol. 17, no. 2, pp. 169–176, 2011.

[15] C. O. Moses, D. K. Nodstrom, and J. S. Herman, "Aqueous pyrite oxidation by dissolved oxygen and by ferric iron," *Geochimica et Cosmochimica Acta*, vol. 51, no. 6, pp. 1561–1571, 1987.

[16] Y. Huai, C. Plackowski, and Y. Peng, "The effect of gold coupling on the surface properties of pyrite in the presence of ferric ions," *Applied Surface Science*, vol. 488, pp. 277–283, 2019.

[17] T. Zhou, Y. Qin, Q. Ma, and J. Liu, "A constitutive model for rock based on energy dissipation and transformation principles," *Arabian Journal of Geosciences*, vol. 12, no. 15, pp. 1–14, 2019.

[18] Y. Wen, C. Xin, X. Zhang et al., "The stability analysis of tunnel lining structure with seismic excitation based on the energy evaluation principle," *Shock and Vibration*, vol. 2021, Article ID 9995682, 17 pages, 2021.

[19] J. Chen, Y. Xuanyuan, and Y. Dai, "Expressions of stored and dissipated energy densities," *Optik*, vol. 207, no. 4, 2020.

[20] F. Gu, D. Presti, M. Heitzman, B. Powell, and V. Allison, "Feasibility of using more polishable aggregates in dense-graded asphalt surface mixture: case study of dolomite," *Construction and Building Materials*, vol. 342, article 127915, 2022.

[21] D. Shiozawa, T. Inagawa, T. Washio, and T. Sakagami, "Accuracy improvement in dissipated energy measurement by using phase information," *Measurement Science and Technology*, vol. 28, 2017.

[22] L. Li, C. Polanco, and A. Ghahreman, "Fe (III)/Fe (II) reduction-oxidation mechanism and kinetics studies on pyrite surfaces," *Journal of Electroanalytical Chemistry*, vol. 774, pp. 66–75, 2016.

[23] Y. Ramprakash, D. Koch, and R. Woods, "The interaction of iron species with pyrite surfaces," *Journal of Applied electrochemistry*, vol. 21, pp. 531–536, 1991.

[24] E. C. Dos Santos, D. Cecí Lia, and H. A. Duarte, "Pyrite oxidation mechanism by oxygen in aqueous medium," *Journal of Physical Chemistry*, vol. 120, no. 5, pp. 2760–2768, 2016.

[25] M. Salamon, "Energy considerations in rock mechanics: fundamental results," *Journal of the Southern African Institute of Mining and Metallurgy*, vol. 84, no. 8, pp. 233–246, 1984.

[26] E. Fjær and H. Ruistuen, "Impact of the intermediate principal stress on the strength of heterogeneous rock," *Journal of Geophysical Research: Solid Earth*, vol. 107, no. B2, 2002.

[27] A. Arisoy and B. Beamish, "Mutual effects of pyrite and moisture on coal self-heating rates and reaction rate data for pyrite oxidation," *Fuel*, vol. 139, pp. 107–114, 2015.

[28] H. Wang, P. A. Dowd, and C. Xu, "A reaction rate model for pyrite oxidation considering the influence of water content and temperature," *Minerals Engineering*, vol. 134, pp. 345–355, 2019.

[29] S. Kaviani, M. Izadyar, and M. R. Housaindokht, "A DFT study on the complex formation between desferrithiocin and metal ions (Mg^{2+}, Al^{3+}, Ca^{2+}, Mn^{2+}, Fe^{3+}, Co^{2+}, Ni^{2+}, Cu^{2+}, Zn^{2+})," *Computational Biology & Chemistry*, vol. 67, pp. 114–121, 2017.

[30] B. G. Tarasov and T. R. Stacey, "Features of the energy balance and fragmentation mechanisms at spontaneous failure of class I and class II rocks," *Rock Mechanics and Rock Engineering*, vol. 50, no. 10, pp. 2563–2584, 2017.

[31] P. Li and M. Cai, "Energy evolution mechanism and failure criteria of jointed surrounding rock under uniaxial compression," *Journal of Central South University*, vol. 28, no. 6, pp. 1857–1874, 2021.

[32] S. Souissi, E. Hamdi, and H. Sellami, "Microstructure effect on hard rock damage and fracture during indentation process," *Geotechnical and Geological Engineering*, vol. 33, no. 6, pp. 1539–1550, 2015.

[33] J.-A. Wang and H. D. Park, "Comprehensive prediction of rockburst based on analysis of strain energy in rocks," *Tunnelling and Underground Space Technology*, vol. 16, no. 1, pp. 49–57, 2001.

[34] M. Aubertin, D. Gill, and R. Simon, "On the use of the brittleness index modified (BIM) to estimate the post-peak behavior of rocks," *Rock Mechanics*, pp. 945–952, 1994.

[35] H. Munoz, A. Taheri, and E. K. Chanda, "Rock drilling performance evaluation by an energy dissipation based on rock brittleness index," *Rock Mechanics and Rock Engineering*, vol. 48, no. 8, pp. 3343–3355, 2016.

[36] M. Jarrahi, G. Blöcher, C. Kluge, and H. M. Holländer, "Elastic–plastic fracture propagation modeling in rock fracturing via punch through shear test," *Rock Mechanics and Rock Engineering*, vol. 54, no. 6, pp. 3135–3147, 2021.

[37] S.-i. Karato and H.-R. Wenk, *Plastic Deformation of Minerals and Rocks (Vol. 51)*, Walter de Gruyter Gmb H & Co KG, 2002.